Strain-induced fast domain wall motion in hybrid piezoelectric-magnetostrictive structures with Rashba and nonlinear dissipative effects

Sumit Maity, Sarabindu Dolui, and Sharad Dwivedi*

Department of Mathematics, School of Sciences, National Institute of Technology Andhra Pradesh, Tadepalligudem 534101, India

The prime objective of this work is to analyze the motion of magnetic domain walls (DWs) in a thin layer of magnetostrictive material that is perfectly attached to the upper surface of a thick piezoelectric actuator. In our analysis, we consider a transversely isotropic hexagonal subclass of magnetostrictive materials that demonstrate structural inversion asymmetry. To this aim, we utilize the one-dimensional extended Landau-Lifshitz-Gilbert equations, which describe the magnetization dynamics under the influence of various factors such as magnetic fields, spin-polarized electric currents, magnetoelastic effects, magnetocrystalline anisotropy, Rashba fields, and nonlinear dry-friction dissipation. By employing the standard traveling wave ansatz, we derive an analytical expression of the most relevant dynamic features: velocity, mobility, threshold, breakdown, and propagation direction of the DWs in both steady and precessional dynamic regimes. Our analytical investigation provides insights into how effectively the considered parameters can control the DW motion. Finally, numerical illustrations of the obtained analytical results show a qualitative agreement with the recent observations.

Domain wall, Magnetoelastic field, Extended Landau-Lifshitz-Gilbert equation, Dry-friction dissipation, Rashba effect

1. Introduction

The investigation of field- and current-induced motion of magnetic domain walls (DWs) in multiferroic heterostructures, driven by applied magnetic fields and electric currents, has gained significant global attention due to its potential applications in various fields such as spintronic memories, sensors, spin-wave filters, and logic gates [1-8]. The development of hybrid piezoelectric-magnetostrictive (PZ-MS) heterostructures has been a focal point in achieving strong magnetoelectric coupling in multiferroic applications. These heterostructures consist of a thin magnetostrictive layer (MSL) firmly attached to the upper surface of a thick piezoelectric layer (PEL). In these composite structures, known as magnetoelectric multiferroics, the external voltage is applied to the PEL, generating an electric field that further induces strains. These strains induced from the PEL are fully moved to the MSL through their shared interface, substantially impacting the magnetic configuration via inverse magnetostrictive effects [2, 7, 9-16]. Due to the combined existence of stress-free strains induced by magnetostriction, the magnetic layer undergoes both direct and inverse magnetostrictive effects [7, 17-23]. Recent observations have shown that the crystal symmetry of the magnetic material significantly impacts the motion of DWs in these heterostructures by affecting anisotropy, magnetoelastic, and magnetostrictive energies [7, 20-22]. Magnetostrictive materials often described in Refs. [2, 7, 20, 24-29] include Co-Pt (platinum-cobalt alloys), Fe-Ga (Galfenol), $Tb_{1-x}Dy_xFe_2$ (terfenol-D), $NiFe_2O_4$, $CoFe_2O_4$, $BaFe_{12}O_{19}$ and other manganites and fer-

rites, whose crystal symmetry generally corresponds to the cubic or hexagonal classes.

Furthermore, it has been observed that the motion of DWs is affected by external stimuli, leading to two distinct dynamic regimes. In the case of low-strength of external stimuli, the DW moves rigidly with a fixed velocity along the major axis, resulting in a steady-state regime. The boundaries of this regime are determined by the threshold and Walker breakdown (WB) limit corresponding to the minimum and maximum values of the external stimuli that allow the motion to remain in the steady-state regime. However, when the strength of the external stimulus surpasses the WB limit, the motion becomes oscillatory due to internal deformation, leading to a precessional regime [7, 13, 14, 17-19, 30, 31].

The DW motion occurring at mesoscale in the MSL is governed by the extended Landau-Lifshitz-Gilbert (ELLG) equation, which includes nonlinear dissipation described via viscous-dry friction mechanism [7, 13, 14, 17-20]. The injection of a spin-polarized electric current into the MSL induces a torque on the magnetization, causing the DW to shift toward the direction of the applied current. This torque is known as spin-transfer torque (STT) [3, 7, 17, 19, 32-36]. In addition to STT, the structural inversion asymmetry of the MSL, which arises from spin-orbit coupling splitting the electronic energy bands, induces a qualitatively distinct spin-orbit torque (SOT). The SOT is mainly due to the Spin-hall and Rashba effects [19, 37-45]. This work specifically focuses on a subclass of transversely isotropic hexagonal materials that exhibit structural inversion asymmetry and comprise the Rashba effect. Recent studies have shown that the Rashba field can significantly modify the DW velocity, mobility, depinning threshold, breakdown, and propagation of DW motion, thereby enabling the development of fast processing speed devices [3, 13, 18, 19, 37, 38, 40].

The present study can be viewed as an extension of recent research on DW motion in hybrid PZ-MS heterostructures for various crystal classes under different scenarios [2, 7, 9, 10, 17-20, 26, 27, 30, 45-49]. It is worth mentioning that these works on such bilayer heterostructures are focused on the flat DWs motion. However, analytical investigation related to the curved DWs in ferromagnetic nanowires/strips can be found in Refs. [37, 50, 51]. In addition, in these works on bilayer heterostructures, the MSL was considered to be either isotropic [17-19, 45-47], cubic [20, 26, 27] or transversely isotropic hexagonal [7] classes of materials. However, devices based on transversely isotropic ferromagnetic materials have proven more advantageous due to their narrow DWs, stable magnetization states, and efficient current-induced DW motion. In Ref. [7], the authors studied DW motion for a transversely isotropic hexagonal class of magnetostrictive materials without the Rashba field and charac-

terized it in steady and precessional dynamic regimes. The present work aims to bridge this gap by focusing on stain-induced DW motion in a transversely isotropic hexagonal magnetostrictive material in the presence of simultaneous effects of magnetocrystalline anisotropy, magnetoelastic, crystal symmetry of the magnetostrictive material, dry friction dissipation, and the Rashba field. To achieve this, we establish explicit functional dependence of the key dynamical features in terms of the considered parameters. Our results are derived assuming that magnetostrictive material is linearly elastic and piezo-induced strains are spatially uniform and fully moved from the PEL into the MSL via a common interface. Due to the elongated and thin geometry of the MSL, we assume that the magnetic DW in the MSL undergoes a one-dimensional motion along the major strip axis. In our model, at the equilibrium, we assume a 180° Bloch-type flat DW, which is initially nucleated at the center of the MSL.

The structure of the paper is as follows. Section 2 presents a theoretical framework to examine the motion of DWs in hybrid PZ-MS heterostructures. This framework utilizes a one-dimensional ELLG equation, which governs the DW motion in steady-state and precessional dynamic regimes. By employing the standard traveling wave ansatz, we obtain an explicit analytical expression of the most significant dynamical entities in terms of the key parameters. Section 3 is devoted to the numerical illustration of the analytical results obtained in Sect. 2. We demonstrate that DW dynamics can be controlled by suitably adjusting the key parameters and provide a qualitative comparison with the existing reference. Finally, in Sect. 4, we conclude this work with plausible remarks.

2. The one dimensional micromagnetic model

We assume an artificial hybrid PZ-MS heterostructure, shown schematically in Fig. 1. The heterostructure comprises a thick PEL and a thin MSL that is perfectly attached to the upper surface of the PEL. We assume the MSL belongs to a subclass of transversely isotropic hexagonal material that depicts structural inversion asymmetry. The dimensions of the MSL, including its length (L), width (w), and thickness (d) along the $\mathbf{e}_1$, $\mathbf{e}_2$, and $\mathbf{e}_3$ axes, respectively, are such that $L >> w > d$. This geometry causes the MSL to form an elongated thin nanostrip. It can be moved along the major axis $\mathbf{e}_1$ via the application of an external bias magnetic field $\mathbf{h}^{\mathrm{app}} = h_1\mathbf{e}_1 + h_2\mathbf{e}_2 + h_3\mathbf{e}_3$ and/or an electric current density $\mathbf{J} = J\mathbf{e}_1$. These stimuli are uniform in space and constant in time. The magnetic field is defined by its components along the $\mathbf{e}_1$, $\mathbf{e}_2$, and $\mathbf{e}_3$ directions, denoted by h_1, h_2, and h_3, respectively, while J represents the strength of the applied current density. The distortion in the PEL is due to an electric voltage
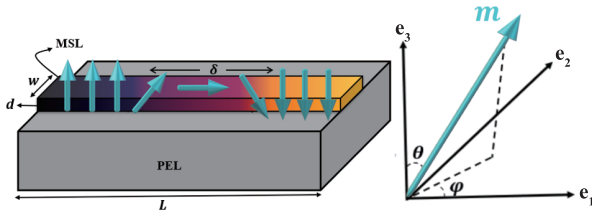
Figure 1   Sketch of a hybrid PZ-MS heterostructure along with the reference axes.

$V^{(P)}$ applied between two electrodes, which in turn induces an electric field directed along the $\mathbf{e}_2$-axis. Due to this induced electric field, the width of the PEL undergoes an elongation (contraction) along with a contraction (elongation) in the other two orthogonal directions. As the PEL and MSL are perfectly bonded, piezo-strains are assumed to be fully moved from the PEL to the MSL through a shared interface.

Next, the Spatio-temporal motion of DW in the ferromagnetic MSL is governed by the ELLG equation [7, 13, 14, 17-20, 26, 27, 52]:

$$\frac{\partial \mathbf{m}}{\partial t} = \mathbf{t}_{\text{prec}} + \mathbf{t}_{\text{diss}} + \mathbf{t}_{\text{stt}} + \mathbf{t}_{\text{ra}}, \tag{1}$$

where, $\mathbf{m} : \mathbb{R} \times \mathbb{R}^+ \rightarrow \mathbb{S}^2$, which represents the normalized magnetization vector. It can be expressed as $\mathbf{m}(x,t) = \mathbf{M}(x,t)/M_s = (m_1, m_2, m_3)$, where m_1, m_2, and m_3 denote the components of $\mathbf{m}$ along the $\mathbf{e}_1$, $\mathbf{e}_2$, and $\mathbf{e}_3$ axes, respectively. Here, we consider that all vector quantity shows a functional dependence on time t as well as on the major axis coordinate $\mathbf{e}_1$, which describes the position along the MSL. This one-dimensional model is well-established in the existing reference, particularly for geometries characterized by thin and elongated structures of the MSL [7, 13, 14, 17-20, 26, 27, 31, 53, 54]. Here, $\mathbb{S}^2$ represents the unit sphere in $\mathbb{R}^3$, $\mathbf{M}(x,t)$ represents the magnetization vector, and M_s corresponds to the saturation magnetization. Furthermore, t and x represent the time and space variables. Also, we have the following torque terms: $\mathbf{t}_{\text{prec}}$, $\mathbf{t}_{\text{diss}}$, $\mathbf{t}_{\text{stt}}$, and $\mathbf{t}_{\text{ra}}$. These terms arise from precession, dissipation, spin-transfer-torque, and the Rashba field.

Next, we provide detailed explanations for each torque term that appears on the right-hand side of Eq. (1). The initial term corresponds to the undamped precessional movement of the magnetization vector around the total effective field $\mathbf{h}_{\text{eff}}$ and can be expressed as

$$\mathbf{t}_{\text{prec}} = \gamma \left(\mathbf{h}_{\text{eff}} \times \mathbf{m} \right), \tag{2}$$

$\gamma = (M_s \mu_0 ge)/m_e$ is a positive constant, where μ_0, g, e, and m_e correspond to the magnetic permeability of the vacuum, Landè factor, electron charge, and mass of the electron, respectively. In our analysis, we assume the collective effects of exchange, demagnetizing, applied, magnetoelastic, and

anisotropy fields when determining the total effective field $\mathbf{h}_{\text{eff}}$ and express it as

$$\mathbf{h}_{\text{eff}} = \mathbf{h}^{\text{ex}} + \mathbf{h}^{\text{dmg}} + \mathbf{h}^{\text{app}} + \mathbf{h}^{\text{me}} + \mathbf{h}^{\text{an}}. \tag{3}$$

The expression for the exchange field $\mathbf{h}^{\text{ex}}$ can be expressed as [17-20, 26, 27]

$$\mathbf{h}^{\text{ex}} = A \frac{\partial^2 \mathbf{m}}{\partial x^2}, \tag{4}$$

where, the constant A is connected with the exchange length l_{ex} and exchange stiffness constant A_{ex} via the relation $A = l_{\text{ex}}^2 = \frac{2A_{\text{ex}}}{\mu_0 M_s^2}$.

The demagnetizing field $\mathbf{h}^{\text{dmg}}$ is considered as [17-20, 26, 27]

$$\mathbf{h}^{\text{dmg}} = -N_1 m_1 \mathbf{e}_1 - N_2 m_2 \mathbf{e}_2 - N_3 m_3 \mathbf{e}_3, \tag{5}$$

where, N_1, N_2, and N_3 represent the demagnetizing factors, obeying the normalization condition $N_1 + N_2 + N_3 = 1$. These factors are determined by the structural geometry of the materials. However, accurately evaluating the demagnetizing field is a highly complex task. Explicit expressions for the demagnetizing field are reported only for a few specific geometries, such as uniformly magnetized ellipsoids [46, 55, 56], straight nanowires with circular cross-sections [57, 58], and nanoscale magnetic tunnel junctions [59, 60]. However, the expression for the demagnetizing field being considered is widely used in the reference as a reliable approximation [17, 19, 20, 26, 27, 31, 46].

Subsequently, the magnetoelastic field in the case of a linear elastic material can be expressed as [7, 17, 20, 21, 26, 27]

$$\mathbf{h}^{\text{me}} = \frac{1}{\mu_0 M_s^2} (\boldsymbol{\epsilon} - \boldsymbol{\epsilon}^\mu) : \mathbb{C} : \frac{\partial \boldsymbol{\epsilon}^\mu}{\partial \mathbf{m}}, \tag{6}$$

where, $\boldsymbol{\epsilon} = \boldsymbol{\epsilon}^e + \boldsymbol{\epsilon}^\mu$, $\boldsymbol{\epsilon}^e$ represents the elastic strain and $\boldsymbol{\epsilon}^\mu = \mathbb{Z} : (\mathbf{m} \otimes \mathbf{m})$ corresponds to the magnetostrictive strain [7, 61-63]. Moreover, ":" denotes the double contraction, "⊗" reflects the tensor product, and $\mathbb{C}$ and $\mathbb{Z}$ correspond to the elasticity and fourth-order magnetostriction tensors, respectively. We consider the MSL of hexagonal crystal classes $\bar{6}$m2, 6mm, 622, and 6/mmm that exhibit transverse isotropy, i.e., invariance under rotations about a certain direction, referred to as axis of symmetry. For such crystals, the elasticity tensor $\mathbb{C}$ depends on five independent elastic constants c_{11}, c_{12}, c_{13}, c_{33} and c_{44}, and in the Voigt notation, as follows

[7, 20, 64]:

$$[\mathbb{C}] = \begin{bmatrix} c_{11} & c_{12} & c_{13} & & & \\ c_{12} & c_{11} & c_{13} & & \mathbf{0} & \\ c_{13} & c_{13} & c_{33} & & & \\ & & & c_{44} & 0 & 0 \\ & \mathbf{0} & & 0 & c_{44} & 0 \\ & & & 0 & 0 & \frac{1}{2}(c_{11} - c_{12}) \end{bmatrix}.$$

It is to remark that for a transversely isotropic material, the fourth-order magnetostriction tensor $\mathbb{Z}$ can be expressed via six independent magnetostriction coefficients

$Z_{1111}, Z_{1122}, Z_{1133}, Z_{2323}, Z_{3311}, Z_{3333}$ [7, 63, 65], and read as

$$[\mathbb{Z}] = \begin{bmatrix} Z_{1111} & Z_{1122} & Z_{1133} & & & \\ Z_{1122} & Z_{1111} & Z_{1133} & & \mathbf{0} & \\ Z_{3311} & Z_{3311} & Z_{3333} & & & \\ & & & Z_{2323} & 0 & 0 \\ & \mathbf{0} & & 0 & Z_{2323} & 0 \\ & & & 0 & 0 & \frac{1}{2}(Z_{1111} - Z_{1122}) \end{bmatrix}. \quad (7)$$

Using Eq. (7), the magnetostriction strain tensor $\boldsymbol{\epsilon}^{\mu}$ can be expressed as [7, 63, 66, 67]

$$\boldsymbol{\epsilon}^{\mu} = \begin{bmatrix} Z_{1111}m_1^2 + Z_{1122}m_2^2 + Z_{1133}m_3^2 & (Z_{1111} - Z_{1122})m_1m_2 & 2Z_{2323}m_1m_3 \\ (Z_{1111} - Z_{1122})m_1m_2 & Z_{1122}m_1^2 + Z_{1111}m_2^2 + Z_{1133}m_3^2 & 2Z_{2323}m_2m_3 \\ 2Z_{2323}m_1m_3 & 2Z_{2323}m_2m_3 & Z_{3311}m_1^2 + Z_{3311}m_2^2 + Z_{3333}m_3^2 \end{bmatrix}. \quad (8)$$

Now, to maintain the standard notation used in recent reports [7, 63, 66-68], we express the magnetostriction coefficients in terms of λ_A, λ_B, λ_C, λ_E, λ_{13}, and λ_{33} by assuming the relation $\lambda_A = Z_{1111} - Z_{1133}$, $\lambda_B = Z_{1122} - Z_{1133}$,

$\lambda_C = Z_{3311} - Z_{3333}$, $\lambda_E = 2Z_{2323}$, $\lambda_{13} = Z_{1133}$, and $\lambda_{33} = Z_{3333}$ [66-68]. Under the aforementioned assumption, Eq. (8), can be recast as

$$\boldsymbol{\epsilon}^{\mu} = \begin{bmatrix} (\lambda_A - \lambda_B)m_1^2 - \lambda_B m_3^2 + \lambda_B + \lambda_{13} & (\lambda_A - \lambda_B)m_1m_2 & \lambda_E m_1m_3 \\ (\lambda_A - \lambda_B)m_1m_2 & (\lambda_A - \lambda_B)m_2^2 - \lambda_B m_3^2 + \lambda_B + \lambda_{13} & \lambda_E m_2m_3 \\ \lambda_E m_1m_3 & \lambda_E m_2m_3 & \lambda_C(1 - m_3^2) + \lambda_{33} \end{bmatrix}. \quad (9)$$

By virtue of Eq. (6), the components of the magnetoelastic field can be derived, and as follows [7, 20, 67, 68]:

$$\begin{aligned} h_1^{\text{me}} = \frac{2}{\mu_0 M_s^2} \Big\{ &(\lambda_A - \lambda_B)\, m_1 \Big[c_{11} \big(\epsilon_{11} - (\lambda_A - \lambda_B)\, m_1^2 \\ &+ \lambda_B m_3^2 - (\lambda_B + \lambda_{13}) \big) + c_{12} \big(\epsilon_{22} - (\lambda_A - \lambda_B)\, m_2^2 \\ &+ \lambda_B m_3^2 - (\lambda_B + \lambda_{13}) \big) + c_{13} \big(\epsilon_{33} + \lambda_C m_3^2 - (\lambda_C \\ &+ \lambda_{33}) \big) \Big] + 2c_{44}\, (\epsilon_{13} - \lambda_E m_1 m_3)\, \lambda_E m_3 + (c_{11} \\ &- c_{12}) (\epsilon_{12} - (\lambda_A - \lambda_B)\, m_1 m_2) (\lambda_A - \lambda_B)\, m_2 \Big\}, \end{aligned}$$

$$\begin{aligned} h_2^{\text{me}} = \frac{2}{\mu_0 M_s^2} \Big\{ &(\lambda_A - \lambda_B)\, m_2 \Big[c_{12} \big(\epsilon_{11} - (\lambda_A - \lambda_B)\, m_1^2 \\ &+ \lambda_B m_3^2 - (\lambda_B + \lambda_{13}) \big) + c_{11} \big(\epsilon_{22} - (\lambda_A - \lambda_B)\, m_2^2 \\ &+ \lambda_B m_3^2 - (\lambda_B + \lambda_{13}) \big) + c_{13} \big(\epsilon_{33} + \lambda_C m_3^2 - (\lambda_C \\ &+ \lambda_{33}) \big) \Big] + 2c_{44} \big(\epsilon_{23} - \lambda_E m_2 m_3 \big) \lambda_E m_3 + \big(c_{11} \\ &- c_{12} \big) \big(\epsilon_{12} - (\lambda_A - \lambda_B)\, m_1 m_2 \big) \big(\lambda_A - \lambda_B \big) m_1 \Big\}, \end{aligned}$$

$$\begin{aligned} h_3^{\text{me}} = \frac{2}{\mu_0 M_s^2} \Big\{ &- \lambda_B m_3 \Big[(c_{11} + c_{12}) \big(\epsilon_{11} + \epsilon_{22} - (\lambda_A \\ &- \lambda_B) \big(m_1^2 + m_2^2 \big) + 2\lambda_B m_3^2 - 2 \big(\lambda_B + \lambda_{13} \big) \big) \\ &+ 2c_{13} \big(\epsilon_{33} + \lambda_C m_3^2 - \lambda_C - \lambda_{33} \big) \Big] \\ &- \lambda_C m_3 \Big[c_{13} \big(\epsilon_{11} + \epsilon_{22} - (\lambda_A - \lambda_B) \big(m_1^2 + m_2^2 \big) \\ &+ 2\lambda_B m_3^2 - 2 \big(\lambda_B + \lambda_{13} \big) \big) + c_{33} \big(\epsilon_{33} + \lambda_C m_3^2 - \lambda_C \\ &- \lambda_{33} \big) \Big] + 2c_{44}\lambda_E \big(\big(\epsilon_{23} - \lambda_E m_2 m_3 \big) m_2 + \big(\epsilon_{13} \\ &- \lambda_E m_1 m_3 \big) m_1 \big) \Big\}. \end{aligned} \quad (10)$$

Next, we elucidate the magnetoelastic field $\mathbf{h}^{\text{me}}$ for the considered hybrid PZ-MS heterostructure. Given the comparatively smaller thickness of the MSL in comparison to the PEL, we can conveniently ignore strain variations along the $\mathbf{e}_3$-axis. As a result, the collective strains affecting the MSL can be ascertained by applying mechanical boundary conditions at both the upper and lower surfaces (in the $\mathbf{e}_1$-$\mathbf{e}_2$ plane)

of the MSL. Based on recent observations, we assume that the in-plane shear strain ϵ_{12} induced by the PEL can be neglected [7, 17, 19, 20, 26, 27]. We further assume that the three planar strains ϵ_{11}, ϵ_{12}, and ϵ_{22} induced by the PEL are fully moved to the MSL through a shared interface between the PEL and MSL. To determine the remaining components of the strain tensor ϵ_{13}, ϵ_{23}, and ϵ_{33}, we apply the traction boundary conditions $\sigma_{ij}n_j = t_i$ at the top surface of the MSL. The null traction $\mathbf{t} = (0, 0, 0)$ acting on the top surface, along with the normal vector $\mathbf{n} = (0, 0, 1)$, yields the following constraints [7, 20]:

$$\sigma_{13} = 0,\ \sigma_{23} = 0,\ \sigma_{33} = 0, \tag{11}$$

where, $\boldsymbol{\sigma} = \mathbb{C} : (\boldsymbol{\epsilon} - \boldsymbol{\epsilon}^\mu)$, denotes the Cauchy stress tensor. Using Eqs. (9) and (11), we obtain [7, 20]

$$\epsilon_{13} = \lambda_E m_1 m_3,\ \epsilon_{23} = \lambda_E m_2 m_3,$$
$$\epsilon_{33} = -\frac{c_{13}}{c_{33}}(\epsilon_{11} + \epsilon_{22}) + \lambda_C(1 - m_3^2) + \lambda_{33}$$
$$+ \frac{c_{13}}{c_{33}}[(\lambda_A + \lambda_B)(1 - m_3^2) + 2\lambda_{13}]. \tag{12}$$

It is worth mentioning that the crystal symmetry of the ferromagnetic material significantly impacts the magnetocrystalline anisotropy field. Thus, for the hexagonal crystals with easy-axis oriented along the $\mathbf{e}_3$-axis, it takes the following form Refs. [2, 7, 20, 67]:

$$\mathbf{h}^{an} = \frac{2K}{\mu_0 M_s^2}(\mathbf{m}.\mathbf{e}_3)\mathbf{e}_3, \tag{13}$$

where K stands for the uniaxial anisotropy coefficient. Also, $\mathbf{h}^{an} = (h_1^{an}, h_2^{an}, h_3^{an})$, where h_1^{an}, h_2^{an}, and h_3^{an} represent the components of $\mathbf{h}^{an}$ along the $\mathbf{e}_1$, $\mathbf{e}_2$, and $\mathbf{e}_3$ directions, respectively.

The subsequent term $\mathbf{t}_{diss}$ consists of two parts and describes the dissipative processes of the system. The first one represents the standard viscous Gilbert-dissipation that describes the dissipative processes in ideal ferromagnets. On the other hand, the second part denotes the dry friction dissipation due to the impurities, dislocations, and crystallographic defects present in the material and captures the pinning effect more realistically [7, 17, 19, 20, 26]:

$$\mathbf{t}_{diss} = \left[\alpha_G + \frac{\gamma\alpha_D}{|\partial\mathbf{m}/\partial t|}\right]\left(\mathbf{m} \times \frac{\partial\mathbf{m}}{\partial t}\right), \tag{14}$$

α_G and α_D represent the classical Gilbert and dry friction dissipation coefficients, respectively.

Next, $\mathbf{t}_{stt}$ represents the STT due to the transfer of spin angular momentum in the MSL. It comprises adiabatic and non-adiabatic contributions, responsible for DW distortion and propagation, respectively [7, 17, 19, 20, 26, 27]

$$\mathbf{t}_{stt} = -u_0 J\frac{\partial\mathbf{m}}{\partial x} - \eta u_0 J\left(\frac{\partial\mathbf{m}}{\partial x} \times \mathbf{m}\right), \tag{15}$$

where η denotes the phenomenological non-adiabatic parameter. Also, $u_0 = (g\mu_B P/2eM_s)$, μ_B, and P correspond to Bohr magneton and current polarization factor, respectively.

Lastly, the term $\mathbf{t}_{ra}$ accounts for the Rashba field arising from the structural inversion asymmetry of the MSL. This term is augmented into the ELLG equation as both a field- and STT-like contribution [3, 18, 19, 26].

$$\mathbf{t}_{ra} = \gamma\hat{\alpha}_{ra}[\mathbf{e}_2 \times \mathbf{m} + \eta\mathbf{m} \times (\mathbf{m} \times \mathbf{e}_2)]J, \tag{16}$$

where, $\hat{\alpha}_{ra} = \alpha_R P/(\mu_0\mu_B M_s^2)$, α_R quantifies the magnitude of the Rashba field.

To characterize the DW motion, we transform the Eq. (1) into a spherical polar framework by assuming the magnetization vector as

$$\mathbf{m} = \cos\varphi\sin\theta\mathbf{e}_1 + \sin\varphi\sin\theta\mathbf{e}_2 + \cos\theta\mathbf{e}_3, \tag{17}$$

where, $\theta(x, t)$ and $\varphi(x, t)$ denote the polar and azimuthal angles, respectively.

By inserting Eq. (17) in Eq. (1), we deduce a pair of partial differential equations of the form:

$$\sin\theta\left(\frac{\partial\varphi}{\partial t}\right) - \left\{\alpha_G + \gamma\alpha_D\left[\left(\frac{\partial\theta}{\partial t}\right)^2 + \sin^2\theta\left(\frac{\partial\varphi}{\partial t}\right)^2\right]^{-1/2}\right\}\left(\frac{\partial\theta}{\partial t}\right)$$
$$= \gamma\left[-A\frac{\partial^2\theta}{\partial x^2} + A\sin\theta\cos\theta\left(\frac{\partial\varphi}{\partial x}\right)^2 - \cos\theta\cos\varphi\left(h_1 + h_1^{me} + h_1^{an}\right)\right.$$
$$- \cos\theta\sin\varphi\left(h_2 + h_2^{me} + h_2^{an}\right) + \sin\theta\left(h_3 + h_3^{me} + h_3^{an}\right)$$
$$+ \sin\theta\cos\theta\left(N_1\cos^2\varphi + N_2\sin^2\varphi - N_3\right) - \hat{\alpha}_{ra}J\cos\theta\sin\varphi$$
$$\left. - \eta\hat{\alpha}_{ra}J\cos\varphi\right] - u_0 J\sin\theta\frac{\partial\varphi}{\partial x} + \eta u_0 J\frac{\partial\theta}{\partial x}, \tag{18}$$

$$\left(\frac{\partial\theta}{\partial t}\right) + \left\{\alpha_G + \gamma\alpha_D\left[\left(\frac{\partial\theta}{\partial t}\right)^2 + \sin^2\theta\left(\frac{\partial\varphi}{\partial t}\right)^2\right]^{-1/2}\right\}\sin\theta\left(\frac{\partial\varphi}{\partial t}\right)$$
$$= \gamma\left[A\sin\theta\frac{\partial^2\varphi}{\partial x^2} + 2A\cos\theta\frac{\partial\theta}{\partial x}\frac{\partial\varphi}{\partial x} + (N_1 - N_2)\sin\theta\sin\varphi\cos\varphi\right.$$
$$+ (h_2 + h_2^{me} + h_2^{an})\cos\varphi - \left(h_1 + h_1^{me} + h_1^{an}\right)\sin\varphi + \hat{\alpha}_{ra}J\cos\varphi$$
$$\left. - \eta\hat{\alpha}_{ra}J\sin\varphi\cos\theta\right] - \eta u_0 J\sin\theta\frac{\partial\varphi}{\partial x} - u_0 J\frac{\partial\theta}{\partial x}. \tag{19}$$

Now, we investigate the DW progression in the steady-state regime, where the DW rigidly propagates with a constant velocity v and a fixed azimuthal angle $\varphi = \varphi_0$ along the longitudinal axis $\mathbf{e}_1$. To this aim, we employ the classical traveling wave ansatz, representing the DW profile as $\theta = \theta(\xi)$, where ξ denotes the traveling wave variable and is defined as $\xi = (x - vt)$. Under these assumptions, we can reformulate Eqs. (18) and (19) as

$$(\alpha_G v - \eta u_0 J)\theta' + \hat{\alpha}_D$$

$$
\begin{aligned}
&= \gamma\Big[-A\theta'' - \cos\theta\cos\varphi_0(h_1 + h_1^{\mathrm{me}} + h_1^{\mathrm{an}}) \\
&\quad - \cos\theta\sin\varphi_0\left(h_2 + h_2^{\mathrm{me}} + h_2^{\mathrm{an}}\right) + \sin\theta\cos\theta\big(N_1\cos^2\varphi_0 \\
&\quad + N_2\sin^2\varphi_0 - N_3\big) + \sin\theta(h_3 + h_3^{\mathrm{me}} + h_3^{\mathrm{an}}) \\
&\quad - \hat{\alpha}_{\mathrm{ra}}J\cos\theta\sin\varphi_0 - \eta\hat{\alpha}_{\mathrm{ra}}J\cos\varphi_0\Big],
\end{aligned} \tag{20}
$$

$$
\begin{aligned}
&(u_0J - v)\,\theta' \\
&= \gamma\Big[(N_1 - N_2)\sin\theta\sin\varphi_0\cos\varphi_0 + (h_2 + h_2^{\mathrm{me}} + h_2^{\mathrm{an}})\cos\varphi_0 \\
&\quad - \left(h_1 + h_1^{\mathrm{me}} + h_1^{\mathrm{an}}\right)\sin\varphi_0 + \hat{\alpha}_{\mathrm{ra}}J\cos\varphi_0 - \eta\hat{\alpha}_{\mathrm{ra}}J\sin\varphi_0\cos\theta\Big],
\end{aligned} \tag{21}
$$

where, $\hat{\alpha}_D = \gamma\alpha_D\mathtt{sign}\left(v\dfrac{\mathrm{d}\theta}{\mathrm{d}\xi}\right)$ and '$\prime$' denotes the derivative with respect to ξ.

Taking into account Eqs. (10), (12), and (13), Eq. (21) renders

$$
\theta' = \Gamma(\sin\theta + \Gamma_1\cos\theta + \Gamma_2), \tag{22}
$$

with

$$
\begin{aligned}
\Gamma = \frac{\gamma}{2(u_0J - v)}\bigg[&(N_1 - N_2) + \frac{2}{\mu_0M_s^2}\,(\lambda_A - \lambda_B) \\
&\cdot (c_{11} - c_{12})\,(\epsilon_{22} - \epsilon_{11})\bigg]\sin 2\varphi_0,
\end{aligned} \tag{23}
$$

$$
\begin{aligned}
\Gamma_1 &= -\,\{2\eta\hat{\alpha}_{\mathrm{ra}}J\sin\varphi_0\}\Bigg/\Bigg\{\bigg[(N_1 - N_2) \\
&\quad + \frac{2}{\mu_0M_s^2}\,(\lambda_A - \lambda_B)(c_{11} - c_{12})(\epsilon_{22} - \epsilon_{11})\bigg]\sin 2\varphi_0\Bigg\} \\
&= -\,\tilde{\Gamma}_1 J,
\end{aligned} \tag{24}
$$

$$
\begin{aligned}
\Gamma_2 &= \{2\,(h_2\cos\varphi_0 - h_1\sin\varphi_0 + \hat{\alpha}_{\mathrm{ra}}J\cos\varphi_0)\}\Bigg/\Bigg\{\bigg[(N_1 - N_2) \\
&\quad + \frac{2}{\mu_0M_s^2}\,(\lambda_A - \lambda_B)(c_{11} - c_{12})(\epsilon_{22} - \epsilon_{11})\bigg]\sin 2\varphi_0\Bigg\} \\
&= \tilde{\Gamma}_2 + \hat{\Gamma}_2 J.
\end{aligned} \tag{25}
$$

Using Eqs. (20) and (22), we fetch the following equation:

$$
\begin{aligned}
&\mathcal{F}_1\sin\theta + \mathcal{F}_2\cos\theta + \mathcal{F}_3\sin\theta\cos\theta + \mathcal{F}_4\sin^2\theta \\
&\quad + \mathcal{F}_5\sin\theta\cos^3\theta + \mathcal{F}_6 = 0,
\end{aligned} \tag{26}
$$

with

$$
\begin{aligned}
\mathcal{F}_1 &= \Gamma(\alpha_G v - \eta u_0 J) - \gamma(h_3 + A\Gamma_1\Gamma_2\Gamma^2), \\
\mathcal{F}_2 &= \Gamma_1\Gamma(\alpha_G v - \eta u_0 J) + \gamma(h_1\cos\varphi_0 + h_2\sin\varphi_0 \\
&\quad + A\Gamma_2\Gamma^2 + \hat{\alpha}_{\mathrm{ra}}J\sin\varphi_0), \\
\mathcal{F}_3 &= \gamma\bigg[A\Gamma^2(1 - \Gamma_1^2) + N_3 - N_2\sin^2\varphi_0 - N_1\cos^2\varphi_0 + \frac{2(\beta - K)}{\mu_0M_s^2}\bigg],
\end{aligned}
$$

$$
\mathcal{F}_4 = -\,2\gamma A\Gamma_1\Gamma^2,
$$

$$
\mathcal{F}_5 = \frac{2\gamma}{\mu_0M_s^2}\left[(\lambda_A^2 + \lambda_B^2)c_{11} + 2\lambda_A\lambda_B c_{12} - \frac{c_{13}^2}{c_{33}}(\lambda_A + \lambda_B)^2\right],
$$

$$
\mathcal{F}_6 = \Gamma_2\Gamma(\alpha_G v - \eta u_0 J) + \hat{\alpha}_D + \gamma A\Gamma_1\Gamma^2 + \gamma\eta\hat{\alpha}_{\mathrm{ra}}J\cos\varphi_0, \tag{27}
$$

where,

$$
\begin{aligned}
\beta &= (\lambda_A - \lambda_B)\bigg[\left(c_{11}\cos^2\varphi_0 + c_{12}\sin^2\varphi_0\right)\epsilon_{11} \\
&\quad + \left(c_{12}\cos^2\varphi_0 + c_{11}\sin^2\varphi_0\right)\epsilon_{22}\bigg] + \bigg[\lambda_B(c_{11} \\
&\quad + c_{12}) - \frac{c_{13}^2}{c_{33}}\,(\lambda_A + \lambda_B)\bigg](\epsilon_{11} + \epsilon_{22}) + \frac{c_{13}^2}{c_{33}}(\lambda_A \\
&\quad + \lambda_B + 2\lambda_{13})\,(\lambda_A + \lambda_B) - \Big[\lambda_A^2 + \lambda_B^2 + \lambda_{13}(\lambda_A \\
&\quad + \lambda_B)\Big]c_{11} - \Big[2\lambda_A\lambda_B + \lambda_{13}\,(\lambda_A + \lambda_B)\Big]c_{12}.
\end{aligned} \tag{28}
$$

To find the explicit expression of the DW width $\delta = \Gamma^{-1}$, we set $\mathcal{F}_3 = 0$ [7, 17-19, 26, 27]

$$
\delta^2 = \Gamma^{-2} = \frac{A_{\mathrm{ex}}\left(1 - \Gamma_1^2\right)}{K - \beta + \dfrac{\mu_0M_s^2}{2}\left(N_1\cos^2\varphi_0 + N_2\sin^2\varphi_0 - N_3\right)}. \tag{29}
$$

Next, we deduce an analytical expression of the traveling wave profile $\theta(\xi)$. We remark that under the constraint $(\Gamma_2^2 - \Gamma_1^2) < 1$, a following meaningful solution of Eq. (22) can be obtained satisfying the symmetry condition $\theta(0) = \pi/2$.

$$
\theta(\xi) = 2\mathtt{arctan}\left[\frac{\Lambda\mu_2\mathtt{exp}(\Gamma\sqrt{1 + \Gamma_1^2 - \Gamma_2^2}\,\xi) - \mu_1}{\Lambda\mathtt{exp}(\Gamma\sqrt{1 + \Gamma_1^2 - \Gamma_2^2}\,\xi) - 1}\right], \tag{30}
$$

where,

$$
\mu_1 = \frac{-1 + \sqrt{1 + \Gamma_1^2 - \Gamma_2^2}}{(\Gamma_2 - \Gamma_1)}, \quad \mu_2 = \frac{-1 - \sqrt{1 + \Gamma_1^2 - \Gamma_2^2}}{(\Gamma_2 - \Gamma_1)}.
$$

By employing the symmetry condition $\theta(0) = \pi/2$, we determine the constant Λ, it yields

$$
\Lambda = \frac{1 + (\Gamma_2 - \Gamma_1)(1 - \Gamma_1) - (\Gamma_2 - \Gamma_1 + 1)\sqrt{1 + \Gamma_1^2 - \Gamma_2^2}}{(\Gamma_2 - \Gamma_1)(\Gamma_2 + 1)}. \tag{31}
$$

It is important to emphasize that in the limit as $|\Gamma_1| \to 0$ and $|\Gamma_2| \to 0$, the solution corresponds to the classical Walker solution, which exhibits a 180° Bloch DW. In this case, the DW profile $\theta(\xi)$ approaches 0 as $\xi \to -\infty$ and π as $\xi \to +\infty$ [7, 17, 19, 20, 26, 27]. However, as we gradually increase the values of $|\Gamma_1|$ and $|\Gamma_2|$, the solution deviates from the classical form, and the magnetization configuration between the distant domains no longer aligns with the $\mathbf{e}_3$-axis. Therefore, without loss of generality, we focus on the cases where

$|\Gamma_1| \simeq 0$ and $|\Gamma_2| \simeq 0$ can be achieved by assuming realistic values for the relevant parameters. Consequently, the DW width (as described by Eq. (29)) shows a weak dependence on the Rashba field and piezo-induced strain, as noted in the recent observations [7, 17, 19, 20, 26, 27]. Thus, the width of the DW is assumed to be constant hereafter.

By taking the average of Eq. (26) over the range of the DW width, i.e., $0 \leq \theta \leq \pi$, we establish the expression of steady DW velocity, as follows:

$$v = \frac{1}{\Gamma \alpha_G \left(2 + \pi \hat{\Gamma}_2 J\right)} \Big[2\gamma h_3 - \hat{\alpha}_D \pi + (2\Gamma \eta u_0 - \gamma \pi \eta \hat{\alpha}_{\mathrm{ra}} \cos \varphi_0) J$$
$$+ \Gamma \left(\pi \eta u_0 \hat{\Gamma}_2 - 2\gamma A \tilde{\Gamma}_1 \hat{\Gamma}_2 \Gamma\right) J^2 \Big]. \tag{32}$$

Let us now characterize the dynamics when the applied magnetic field $\mathbf{h}^{\mathrm{app}}$ and an electric current $\mathbf{J}$ act individually to explore the impact of the external stimuli on the DW velocity. In the case of field-driven DW motion, the DW velocity undergoes a linear upward, causing the DW to move along the major axis $\mathbf{e}_1$. On the contrary, in current-induced DW motion, the presence of the Rashba field introduces a non-zero coefficient $|\Gamma_1|$, resulting in a non-linear variation of the DW velocity with the electric current. Moreover, the Rashba field also affects the DW velocity, the modulus and sign of the DW mobility ($\partial v / \partial J$), and the propagation direction of DW motion. In fact, the direction of DW motion changes at a critical value of the Rashba coefficient ($\hat{\alpha}_{\mathrm{ra}} = \hat{\alpha}_{\mathrm{ra}}^*$), which can be expressed as

$$\hat{\alpha}_{\mathrm{ra}}^* = \frac{\pi u_0}{2\gamma A \Gamma} \Big[N_1 - N_2 + \frac{2}{\mu_0 M_s^2}(\lambda_A - \lambda_B)(c_{11}$$
$$- c_{12})(\epsilon_{22} - \epsilon_{11}) \Big] \cos \varphi_0. \tag{33}$$

As a result, a forward (backward) motion is observed when $\hat{\alpha}_{\mathrm{ra}} < \hat{\alpha}_{\mathrm{ra}}^*$ ($\hat{\alpha}_{\mathrm{ra}} > \hat{\alpha}_{\mathrm{ra}}^*$). We remark that the change in the direction of motion also affects the coefficient of dry friction, $\hat{\alpha}_D$, while the traveling wave profile $\theta(\xi)$ remains unchanged.

The lower limit of the steady-state regime, referred to as the threshold limit, corresponds to the minimum value of the external stimuli to overcome the pinning effects. Now, we determine the threshold value of the applied magnetic field h_3 and electric current density J by using the Eq. (32):

$$J = 0 \Rightarrow h_3^{(\mathrm{th})} = \frac{\pi}{2\gamma} \hat{\alpha}_D, \tag{34}$$

for the range $\hat{\alpha}_{\mathrm{ra}} \gtrless \hat{\alpha}_{\mathrm{ra}}^*$ and $h_3 = 0$, we obtain

$$J^{(\mathrm{th})} = \frac{1}{2\hat{\Gamma}_2 \Gamma \left(\pi \eta u_0 - 2\gamma A \tilde{\Gamma}_1 \Gamma\right)} \Big\{ \gamma \pi \eta \hat{\alpha}_{\mathrm{ra}} \cos \varphi_0$$
$$- 2\Gamma \eta u_0 \mp \Big[(2\Gamma \eta u_0 - \gamma \pi \eta \hat{\alpha}_{\mathrm{ra}} \cos \varphi_0)^2$$
$$+ 4\hat{\Gamma}_2 \Gamma \left(\pi \eta u_0 - 2\gamma A \tilde{\Gamma}_1 \Gamma\right) \pi \hat{\alpha}_D \Big]^{1/2} \Big\}. \tag{35}$$

It is evident from Eqs. (34) and (35), the depinning threshold depends only on the nonlinear dissipation coefficient for the field-driven DW motion. On the other hand, the threshold can be manipulated via the Rashba field, piezo-induced strains, and nonlinear damping coefficient for the current-driven DW motion.

The upper limit of the steady-state regime, known as the WB limit, is derived from Eq. (32) and yields the following DW velocity constraints:

$$J = 0 \Rightarrow v \leq v^*, \tag{36}$$

$$h_3 = 0 \Rightarrow \begin{cases} v \leq u_0 J + v^*, & \text{for} \quad \hat{\alpha}_{\mathrm{ra}} < \hat{\alpha}_{\mathrm{ra}}^*, \\ v \geq u_0 J - v^*, & \text{for} \quad \hat{\alpha}_{\mathrm{ra}} > \hat{\alpha}_{\mathrm{ra}}^*, \end{cases} \tag{37}$$

$$v^* = \frac{\gamma \delta}{2} \Big[N_1 - N_2 + \frac{2}{\mu_0 M_s^2}(\lambda_A - \lambda_B)(c_{11} - c_{12})(\epsilon_{22} - \epsilon_{11}) \Big]. \tag{38}$$

Now, we establish the WB limit for the external magnetic field and electric current density by using Eqs. (32) and (37). It takes the following form:

$$h_3^{\mathrm{WB}} = \frac{\alpha_G}{2} \Big| N_1 - N_2 + \frac{2}{\mu_0 M_s^2}(\lambda_A - \lambda_B)(c_{11}$$
$$- c_{12})(\epsilon_{22} - \epsilon_{11}) \Big| + \frac{\pi}{2\gamma} \hat{\alpha}_D. \tag{39}$$

For the current-induced motion, the WB limit depends on the critical value of the Rashba parameter. To be precise, for forward (backward) motion, the WB limit is represented as $J_{\mathrm{upper}}^{\mathrm{WB}}$ $\left(J_{\mathrm{lower}}^{\mathrm{WB}}\right)$. For forward motion, i.e., $\hat{\alpha}_{\mathrm{ra}} < \hat{\alpha}_{\mathrm{ra}}^*$

$$J_{\mathrm{upper}}^{\mathrm{WB}} = \frac{1}{2((\eta - \alpha_G)u_0 \pi \hat{\Gamma}_2 - 2\gamma A \tilde{\Gamma}_1 \hat{\Gamma}_2)} \Big\{ \big(2u_0(\alpha_G$$
$$- \eta) + \gamma \pi \delta \eta \hat{\alpha}_{\mathrm{ra}} \cos \varphi_0 + \alpha_G v^* \pi \hat{\Gamma}_2 \big) + \big[\big(2u_0(\alpha_G - \eta)$$
$$+ \gamma \pi \delta \eta \hat{\alpha}_{\mathrm{ra}} \cos \varphi_0 + \alpha_G v^* \pi \hat{\Gamma}_2 \big)^2 + 4\big((\eta - \alpha_G)u_0 \pi \hat{\Gamma}_2$$
$$- 2\gamma A \Gamma \tilde{\Gamma}_1 \hat{\Gamma}_2 \big)\big(\pi \delta \hat{\alpha}_D + 2\alpha_G v^* \big) \big]^{1/2} \Big\}. \tag{40}$$

For backward motion, i.e., $\hat{\alpha}_{\mathrm{ra}} > \hat{\alpha}_{\mathrm{ra}}^*$

$$J_{\mathrm{lower}}^{\mathrm{WB}} = \frac{1}{2((\eta - \alpha_G)u_0 \pi \hat{\Gamma}_2 - 2\gamma A \tilde{\Gamma}_1 \hat{\Gamma}_2)} \Big\{ \big(2u_0(\alpha_G$$
$$- \eta) + \gamma \pi \delta \eta \hat{\alpha}_{\mathrm{ra}} \cos \varphi_0 - \alpha_G v^* \pi \hat{\Gamma}_2 \big) - \big[\big(2u_0(\alpha_G - \eta)$$
$$+ \gamma \pi \delta \eta \hat{\alpha}_{\mathrm{ra}} \cos \varphi_0 - \alpha_G v^* \pi \hat{\Gamma}_2 \big)^2 + 4\big((\eta - \alpha_G)u_0 \pi \hat{\Gamma}_2$$
$$- 2\gamma A \Gamma \tilde{\Gamma}_1 \big)\big(\pi \delta \hat{\alpha}_D - 2\alpha_G v^* \big) \big]^{1/2} \Big\}. \tag{41}$$

Eqs. (40) and (41) indicate that the WB limits are affected by the Rashba field, piezo-induced strain, and dry friction coefficient. As the magnitude of the external stimuli exceeds the WB limit, the motion is no longer steady and becomes oscillatory, referred to as a precessional dynamic regime.

Next, we characterize the precessional regime. In this case, the DW motion is described via time-varying velocity $v(t)$ and periodic oscillations at microwave frequency with constant angular speed $\dot{\varphi} = \omega_0$. The system of Eqs. (18) and (19) reads as

$$\sin\theta\omega_0 + \left\{\alpha_G v + \gamma\alpha_D v\left[v^2(\theta')^2 + \omega_0^2\sin^2\theta\right]^{-1/2} - \eta u_0 J\right\}\theta'$$
$$= \gamma\left[-A\theta'' - \cos\theta\cos\varphi(h_1 + h_1^{\mathrm{me}} + h_1^{\mathrm{an}}) - \cos\theta\sin\varphi(h_2\right.$$
$$+ h_2^{\mathrm{me}} + h_2^{\mathrm{an}}) + \sin\theta(h_3 + h_3^{\mathrm{me}} + h_3^{\mathrm{an}}) + \sin\theta\cos\theta(N_1\cos^2\varphi$$
$$\left.+ N_2\sin^2\varphi - N_3) - \hat{\alpha}_{\mathrm{ra}}J\cos\theta\sin\varphi - \eta\hat{\alpha}_{\mathrm{ra}}J\cos\varphi\right], \quad (42)$$

$$(u_0 J - v)\theta' + \left\{\alpha_G + \gamma\alpha_D\left[v^2(\theta')^2 + \omega_0^2\sin^2\theta\right]^{-1/2}\right\}\sin\theta\omega_0$$
$$= \gamma\left[(N_1 - N_2)\sin\theta\sin\varphi\cos\varphi + (h_2 + h_2^{\mathrm{me}} + h_2^{\mathrm{an}})\cos\varphi\right.$$
$$\left.- (h_1 + h_1^{\mathrm{me}} + h_1^{\mathrm{an}})\sin\varphi + \hat{\alpha}_{\mathrm{ra}}J\cos\varphi - \eta\hat{\alpha}_{\mathrm{ra}}J\sin\varphi\cos\theta\right].$$
$$(43)$$

Now, we evaluate all dynamic entities at the center of the DW, where $\theta = \pi/2$, while assuming that the traveling wave profile (22) remains constant. With these considerations, Eqs. (42) and (43) can be expressed as

$$\omega_0 + \Gamma\left[\alpha_G + \gamma\alpha_D\left(v^2\Gamma^2 + \omega_0^2\right)^{-1/2}\right]v$$
$$= \gamma h_3 + \Gamma\eta u_0 J - \gamma\eta\hat{\alpha}_{\mathrm{ra}}J\cos\varphi, \quad (44)$$
$$\left[\alpha_G + \gamma\alpha_D\left(v^2\Gamma^2 + \omega_0^2\right)^{-1/2}\right]\omega_0$$
$$= \Gamma(v - u_0 J) + \gamma\sin\varphi_0\cos\varphi_0\left[(N_1 - N_2)\right.$$
$$\left.+ \frac{2}{\mu_0 M_s^2}(\lambda_A - \lambda_B)(c_{11} - c_{12})(\epsilon_{22} - \epsilon_{11})\right]$$
$$+ \gamma\hat{\alpha}_{\mathrm{ra}}J\cos\varphi. \quad (45)$$

By taking the average of Eqs. (44) and (45) over the precession period and making the further physical assumption that $\Gamma v_a \ll \omega_0$ to achieve the explicit expression of the average DW velocity. This assumption is reasonable based on the typical reference values of precessional angular frequency and DW width. Consequently, we deduce

$$\omega_0 + \alpha_G\Gamma v_a = \gamma h_3 + \Gamma\eta u_0 J, \quad (46)$$
$$\alpha_G\omega_0 + \gamma\alpha_D = \Gamma(v_a - u_0 J). \quad (47)$$

By eliminating the parameter ω_0 from the above two Eqs. (46) and (47), we obtain the following expression for the average velocity of the DW, denoted as v_a.

$$v_a = \frac{\alpha_G\gamma\delta}{1 + \alpha_G^2}h_3 + \frac{(1 + \alpha_G\eta)u_0}{1 + \alpha_G^2}J + \frac{\gamma\delta}{1 + \alpha_G^2}\alpha_D. \quad (48)$$

Eq. (48) reveals that the average velocity of the DW remains unaffected by changes in the Rashba parameter. Furthermore, in contrast to the steady-state regime, where piezo-induced strains influence field-driven and current-driven DW

mobilities, the impact is distinct here. To be precise, the piezo-induced strains affect the filed-driven DW mobility ($\partial v_a/\partial h_3$); however, the current-driven DW mobility ($\partial v_a/\partial J$) remains unaffected.

3. Numerical results

In this section, we present the numerical illustrations of the analytical results derived in the previous section and provide qualitative comparison by assuming realistic parameter values from the Refs. [2, 7, 19, 21, 26, 67, 69-72]. We consider the MSL having length $L = 20$ μm, width $w = 700$ nm, and thickness $d = 20$ nm along the axes $\mathbf{e}_1$, $\mathbf{e}_2$, and $\mathbf{e}_3$, respectively, and satisfying constrain $L >> w > d$. In our analysis, we use the parameter for hexagonal cobalt-based alloy. More precisely, the set of parameters comprises the following values: the exchange constant A_{ex} is 14 pJ/m, the demagnetizing factors are $N_1 = 0.6417$, $N_2 = 0.0093$, and $N_3 = 0.3490$, the saturation magnetization M_s is 1.2971 A/m, the dimensionless Gilbert damping constant α_G is 0.01, the current polarization factor P is 0.45, the elastic constants are $c_{11} = 320$ GPa, $c_{12} = 190$ GPa, $c_{13} = 265$ GPa, $c_{33} = 330$ GPa, and $c_{44} = 75$ GPa. Also, the non-adiabatic coefficient η is 0.5, the anisotropy coefficient K is 2×10^5 J/m^3, and the magnetostriction coefficients are $\lambda_A = -45 \times 10^{-6}$, $\lambda_B = -95 \times 10^{-6}$, $\lambda_C = +110 \times 10^{-6}$, $\lambda_E = -232 \times 10^{-6}$, $\lambda_{13} = -580 \times 10^{-6}$, and $\lambda_{33} = 1.002 \times 10^{-3}$ [21, 67, 69-72]. We assume that the out-of-plane strain ϵ_{33} takes values in the range $(-4, +10) \times 10^{-4}$ and $\varphi_0 = 10°$ [7]. In addition, we consider the dry friction coefficient α_D is dependent on the strains via the relation $\alpha_D = (1 - \nu\epsilon_{33}) \times 10^{-3}$, with $\nu = 500$ or 0, as suggested in Ref. [7]. It is evident from Eq. (12) that the out-of-plane strain ϵ_{33} depends on the piezo-induced strains ϵ_{11} and ϵ_{22}. We remark that the dependence of the dry friction coefficient on piezo-induced strains is also considered in the works presented in Refs. [17, 19, 26, 27].

In Fig. 2 (a) and (b), we inspected the traveling wave profile θ for varying Rashba parameter α_R and fixed out-of-plane strain ε_{33} and vice-versa, respectively. For a constant value of ε_{33} and in the absence of the Rashba field, the traveling wave profile attains the classical walker solution, i.e., $\theta(-\infty) \approx 0$ and $\theta(+\infty) \approx \pi$, which is associated with a 180° Bloch DW [17,19,20]. Moreover, the profile shifts away from the classical form as we gradually increase the Rashba parameter. On the other hand, for fixed α_R, the traveling wave profile depicts negligible dependence on the out-of-plane strain (Fig. 2(b)). In Fig. 3, we gain the insight of out-of-plane strain dependence of DW width for varying the Rashba parameter reflecting forward ($\hat{\alpha}_{\mathrm{ra}} < \hat{\alpha}_{\mathrm{ra}}^*$) and backward ($\hat{\alpha}_{\mathrm{ra}} > \hat{\alpha}_{\mathrm{ra}}^*$) motion. For fixed α_R, the DW width shows an upward shift and
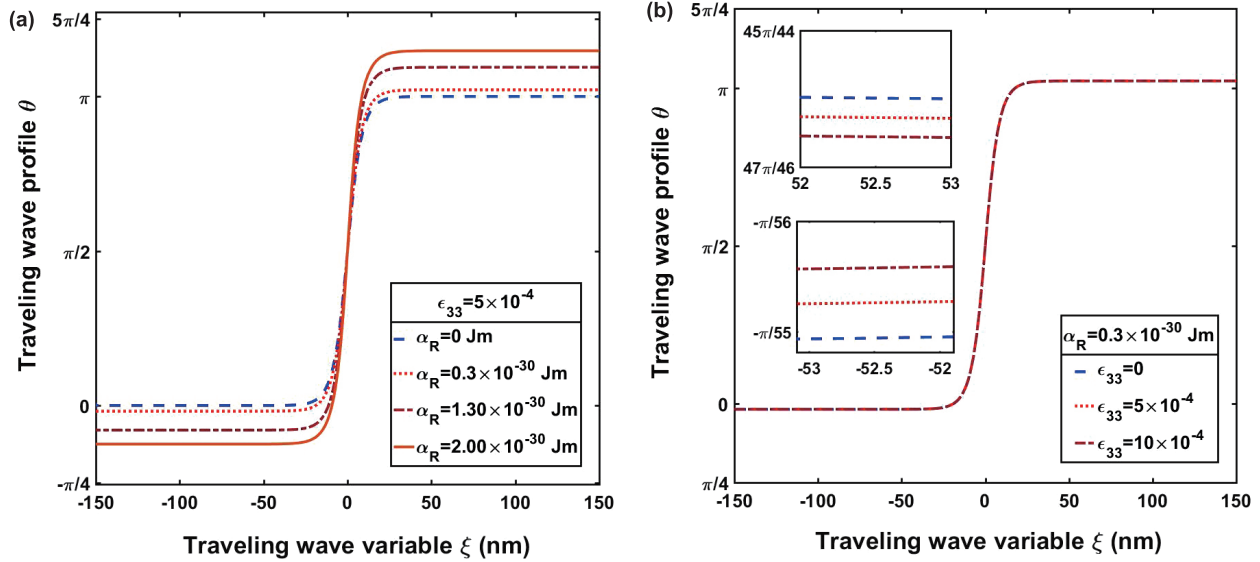
Figure 2 Traveling wave profile $\theta(\xi)$ obtained for (a) varying Rashba parameter α_R and fixed out-of-plane strain ε_{33}, and (b) vice-vesra.

varies linearly with the out-of-plane strain ϵ_{33}. Moreover, for $\hat{\alpha}_{\mathrm{ra}} < \hat{\alpha}_{\mathrm{ra}}^*$, there is no significant variation in the DW width, as shown in the inset. However, the DW width decreases as the Rashba parameter exceeds the critical value. Also, the crystal symmetry impacts the DW width via the magnetoe-lastic field and the magnetocrystalline anisotropy. Such behavior is also observed in the previous works presented in Refs. [7, 26]. Moreover, the dependence of the depinning threshold and WB limit of the external magnetic field with the out-of-plane strain ϵ_{33} have been illustrated in Fig. 4. We notice that the threshold and the WB limit decrease as we gradually increase the out-of-plane strain. This decreas-ing behavior of the threshold with the strain is also noticed in Ref. [20], wherein the MSL is considered to be of cubic crystal classes.

Now, we characterize the boundaries of the steady-state regime for the current-induced DW motion. In Fig. 5, we present the plot of the threshold electric current density $J^{(\mathrm{th})}$ with the out-of-plane strain ϵ_{33} for varying the Rashba pa-rameter α_R. For forward DW motion with a fixed α_R, the threshold current density exhibits a linear decrease as ε_{33} in-creases. However, when ε_{33} is held constant, an increase in the Rashba parameter results in an upward shift in the depin-ning threshold of the current density. Moreover, for the back-ward DW motion, the threshold value of the current density remains unchanged and demonstrates a weak dependence on both α_R and ε_{33}, as observed in the inset of Fig. 5.

Furthermore, the dependence of the WB limit of current density on the out-of-plane strain for varying the Rashba pa-rameter has been portrayed in Fig. 6(a) and (b). In particular, Fig. 6(a) and (b) delineate the forward (backward) DW mo-tion in which the WB limit is identified as $J_{\mathrm{upper}}^{\mathrm{WB}}$ ($J_{\mathrm{lower}}^{\mathrm{WB}}$). For
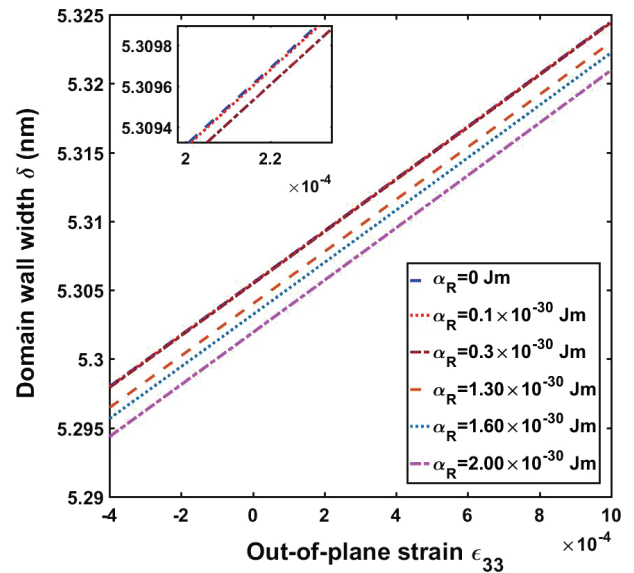

Figure 3 Schematics of a bilayer PZ-MS heterostructure along with the reference axes.

the forward DW motion and the fixed α_R, it decreases linearly with the increase of out-of-plane strain ϵ_{33}, whereas for the fixed ϵ_{33}, it increases as we increase the Rashba parameter. On the contrary, for the backward motion and fixed α_R, the WB limit of electric current density increases linearly with the out-of-plane strain ϵ_{33}. Also, it decreases as we increase the Rashba parameter for the fixed ε_{33}. These results indicate that the steady-state regime can be adjusted by suitably tun-ing the Rasbha parameter and the out-of-plane strain. Such qualitative trends of the threshold and WB values of applied fields have also been observed for isotropic and cubic crys-tal classes of the MSLs in these heterostructures under the Rashba effect in Refs. [19, 26]. In Fig. 7, we characterize
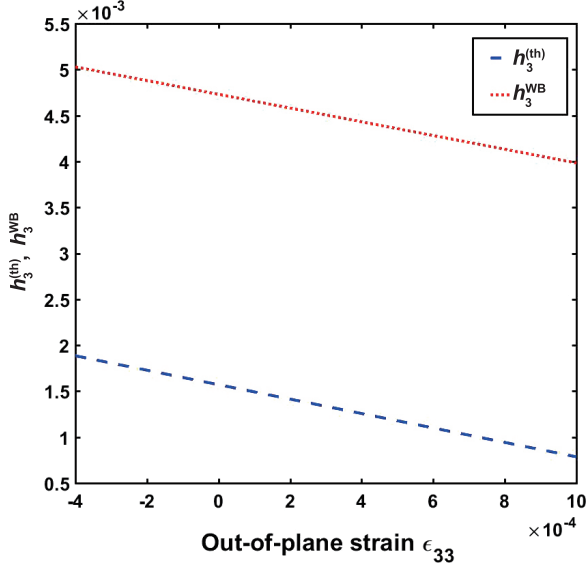
Figure 4 Out-of-plane strain ϵ_{33} dependence of the threshold $h_3^{(\text{th})}$ and WB h_3^{WB} limits of applied magnetic field h_3.
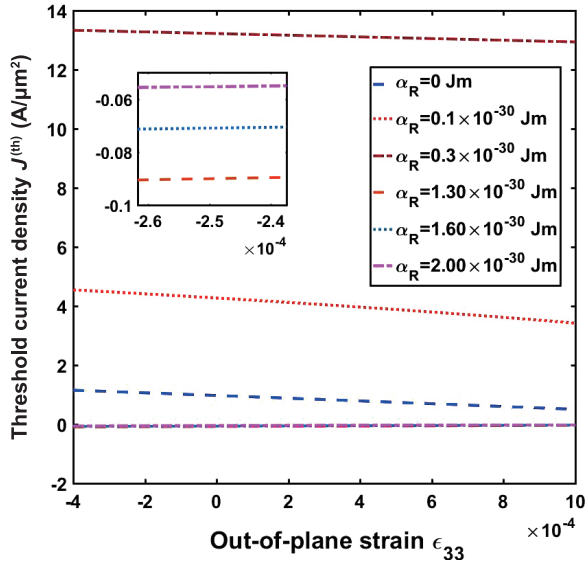
Figure 5 Dependence of threshold current density $J^{(\text{th})}$ on the out-of-plane strain ϵ_{33} for varying Rashba parameter α_R.

Figure 6 Dependence of the WB limit of current density on out-of-plane strain ϵ_{33} for the different values of α_R (a) forward motion ($\hat{\alpha}_{\text{ra}} < \hat{\alpha}_{\text{ra}}^*$), and (b) backward motion ($\hat{\alpha}_{\text{ra}} > \hat{\alpha}_{\text{ra}}^*$).

the field-induced DW dynamics and delineate the strain-dependent DW velocity v with an external magnetic field h_3. It is observed that the velocity of the DW increases linearly with an external magnetic field for fixed ε_{33}. However, for the constant applied magnetic field, it is possible to achieve high velocities as we gradually increase the out-of-plane strain. A similar observation is also noticed without considering the Rashba parameter in Refs. [2,7].

In Figs. 8 and 9, we present the current-induced DW dynamics and illustrate the velocity profile for varying Rashba parameters, fixed out-of-plane strain, and vice-versa. In particular, we investigate the dependence of DW velocity on the

electric current density for the constant out-of-plane strain and varying Rashba parameter for forward (Fig. 8(a)) and backward motion (Fig. 8(b)). For the forward motion ($v \geq 0$) and the fixed Rashba parameter, the DW velocity v increases with the current density J, as shown in Fig. 8(a). Furthermore, for the fixed J, the DW mobility ($\partial v/\partial J$) decreases with an increase in the Rashba parameter. Also, a larger Rashba field leads to higher velocities, with the corresponding WB limit shifted upward. However, for the backward motion ($v < 0$), the DW mobility changes sign, and the direction of motion is reversed, as apparent from Fig. 8(b). Consequently, increasing the Rashba parameter increases DW mobility, and a higher magnitude of DW velocities (in an absolute sense) can be attained even for small current values.

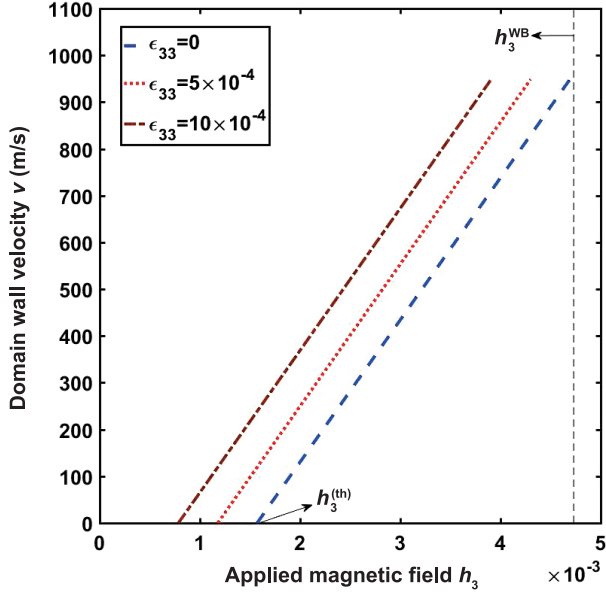Figure 9 (a) and (b) exhibit the relationship between the

Figure 7 Profile of DW velocity v versus applied magnetic field h_3 for varying out-of-plane strain ϵ_{33}.

DW velocity and current density, considering different values of out-of-plane strain and a fixed Rashba parameter. These figures depict both the forward and backward motion of the DW. It is observed that the out-of-plane strain does not impact the mobility of the DW; however, it expands the steady-state regime. Furthermore, the influence of out-of-plane strain on the DW velocities is more significant during backward motion than the forward one. It is to emphasize that a similar trend in DW velocity under the action of the Rashba field is also reported in previous studies [19, 26] concerning isotropic and cubic crystal classes magnetostrictive materials under the Rashba effect.

Finally, the field- and current-induced DW motion in the precessional regime have been exhibited in Fig. 10 (a) and (b), respectively. In Fig. 10 (a), we represent the variation of the average velocity v_a of the DW with the applied magnetic field h_3 for varying out-of-plane strain ϵ_{33}. For the fixed strain, we observe that the average velocity of the DW increases linearly with the magnetic field. However, for a fixed external magnetic field, it decreases with an increase in ϵ_{33}. Moreover, Fig. 10(b) shows the average velocity of the DW as a function of current density J for varying out-of-plane strain ϵ_{33}. The average velocity of the DW increases linearly with the current density. Also, it admits weak dependence on the out-of-plane strain. It is worth remarking that the average velocity of the DW is affected by the Rashba field via the DW width (Eq. (48)). Since the width of the DW is weakly reliant on the Rashba field; as a result, the average velocity remains unaffected by tuning the Rashba parameter. It shows a qualitative agreement with the recent theoretical studies reported in Refs. [18, 26].
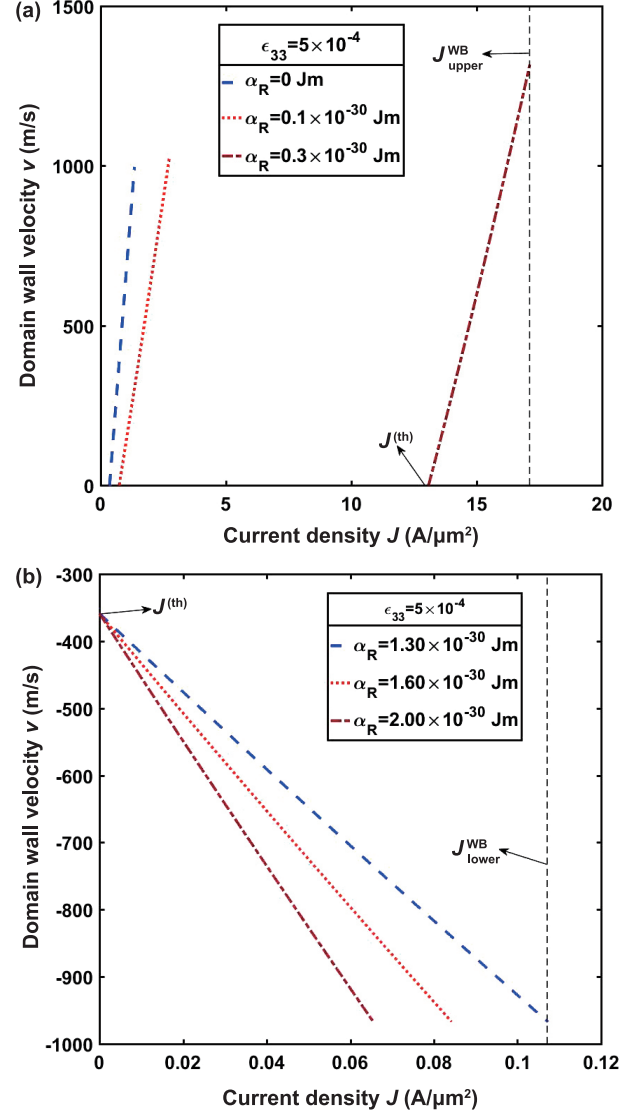

Figure 8 Profile of DW velocity v versus current density J for constant ε_{33} and different values of α_R (a) forward motion ($\hat{\alpha}_{ra} < \hat{\alpha}_{ra}^*$), and (b) backward motion ($\hat{\alpha}_{ra} > \hat{\alpha}_{ra}^*$).

Lastly, it is worth mentioning that the theoretical findings presented in this study are at par with recent observations [2, 3, 7, 9, 10, 18-20, 26, 30, 48]. These studies provide empirical evidence for achieving versatile control over DW mobility. More precisely, they demonstrate that adjusting the Rashba parameter and piezo-induced strains makes it possible to modulate both the DW velocity, threshold, and WB limit.

4.　Conclusions

In a nutshell, this work deals with an analytical investigation of strain-induced fast DW motion in a hybrid PZ-MS heterostructure by considering the combined influence of various factors, including applied magnetic fields, spin-
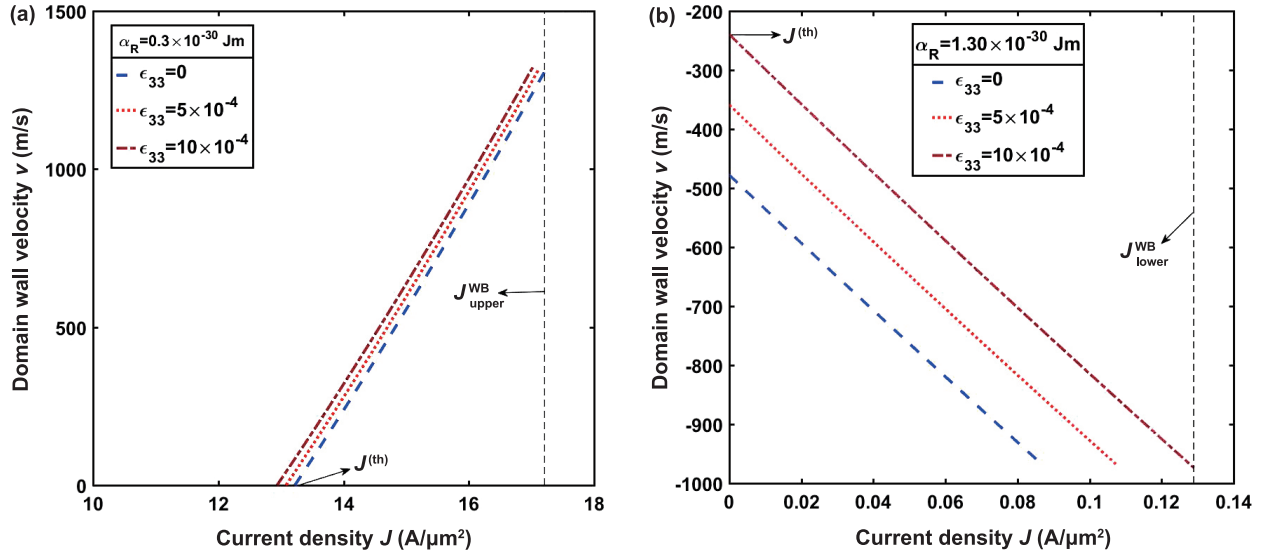
Figure 9 Profile of the DW velocity *v versus* current density *J* for constant α_R and different values of ϵ_{33} (a) forward motion ($\hat{\alpha}_{ra} < \hat{\alpha}_{ra}^*$), and (b) backward motion ($\hat{\alpha}_{ra} > \hat{\alpha}_{ra}^*$).
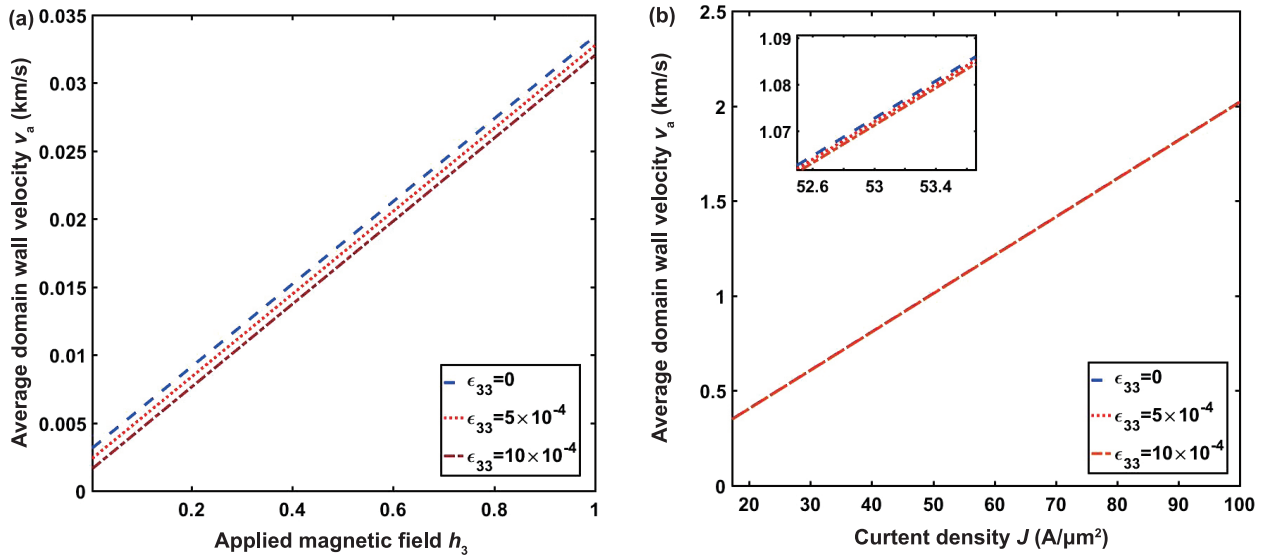

Figure 10 Dependence of average velocity v_a of the DW for varying out-of-plane strain ϵ_{33} on (a) applied magnetic field h_3, (b) electric current density J.

polarized currents, magnetoelastic effects, magnetocrystalline anisotropy, nonlinear dry friction dissipation, Rashba fields, and the crystal symmetry of the ferromagnetic material. Furthermore, it is assumed that the MSL belongs to a subclass of transversely isotropic hexagonal crystal class that exhibits structural inversion asymmetry. The analysis is carried out by assuming the linear elasticity for the MSL and considering that the piezo-induced strains are spatially homogeneous and fully moved from the PEL to the MSL through their shared interface.

We analyzed using the ELLG equation framework and obtained an explicit analytical expression for the key features

of DW motion in both dynamic regimes. Our findings reveal that piezo-induced strains and the Rashba field significantly impact expanding the steady-state regime, leading to higher DW velocities. The relationship between DW velocity and external stimuli remains linear in the presence of dry friction and piezo-induced strains. However, the introduction of the Rashba field introduces nonlinearity. Additionally, by appropriately adjusting factors such as piezo-induced strains, electric current density, Rashba, and dry friction coefficients, the average velocity of the DW can be modulated.

In summary, our findings suggest that the Rashba field provides an additional control parameter through which the DW

motion in the considered bilayer structure can be suitably manipulated. More precisely, our observations exhibit that the velocity of the DW increases with the increase of the Rashba field. In addition, the presence of the Rashba parameter results in a higher WB limit of the applied current density. These observations hold significant promise for developing high-performance and energy-efficient DW-based devices.

Finally, we emphasize that the obtained results in this study demonstrate a qualitative agreement with the existing reference. The previous works have investigated the DW motion wherein the impact of the relevant key parameters was considered separately. However, our approach involves the holistic consideration of these parameters, enabling us to present a thorough analysis that unveils the interrelationships and cumulative influence of these factors on the system's dynamics. In our future work, we intend to extend the present study to further research lines that include (1) investigating fast DW motion in PZ-MS heterostructures for various crystal classes of magnetostrictive materials such as trigonal, tetragonal, orthorhombic, etc. (2) spinorbitronic technologies, where thin MS layers exhibit perpendicular anisotropy, Spin-Hall effect, and Dzyaloshinskii-Moriya interaction (3) strain-controlled curved DW motion in such heterostructures.

1 S. Ratha, M. Kuppan, G. Egawa, and S. Yoshimura, Excellent magnetic properties in multiferroic BiFeO$_3$ based thin films for magnetic devices application, Nano-Struct. Nano-Objects **35**, 101007 (2023).

2 P. M. Shepley, A. W. Rushforth, M. Wang, G. Burnell, and T. A. Moore, Modification of perpendicular magnetic anisotropy and domain wall velocity in Pt/Co/Pt by voltage-induced strain, Sci. Rep. **5**, 7921 (2015), arXiv: 1408.2664.

3 I. M. Miron, T. Moore, H. Szambolics, L. D. Buda-Prejbeanu, S. Auffret, B. Rodmacq, S. Pizzini, J. Vogel, M. Bonfim, A. Schuhl, and G. Gaudin, Fast current-induced domain-wall motion controlled by the Rashba effect, Nat. Mater. **10**, 419 (2011).

4 K. L. Wang, J. G. Alzate, and P. Khalili Amiri, Low-power non-volatile spintronic memory: STT-RAM and beyond, J. Phys. D-Appl. Phys. **46**, 074003 (2013).

5 R. Gupta, and R. K. Kotnala, A review on current status and mechanisms of room-temperature magnetoelectric coupling in multiferroics for device applications, J. Mater. Sci. **57**, 12710 (2022).

6 W. Eerenstein, N. D. Mathur, and J. F. Scott, Multiferroic and magnetoelectric materials, Nature **442**, 759 (2006).

7 G. Consolo, S. Federico, and G. Valenti, Magnetostriction in transversely isotropic hexagonal crystals, Phys. Rev. B **101**, 014405 (2020).

8 Y. Yang, M. Li, and F. Xu, A 3D hard-magnetic rod model based on co-rotational formulations, Acta Mech. Sin. **38**, 222085 (2022).

9 N. Lei, T. Devolder, G. Agnus, P. Aubert, L. Daniel, J. V. Kim, W. Zhao, T. Trypiniotis, R. P. Cowburn, C. Chappert, D. Ravelosona, and P. Lecoeur, Strain-controlled magnetic domain wall propagation in hybrid piezoelectric/ferromagnetic structures, Nat. Commun. **4**, 1378 (2013).

10 T. Mathurin, S. Giordano, Y. Dusch, N. Tiercelin, P. Pernod, and V. Preobrazhensky, Stress-mediated magnetoelectric control of ferromagnetic domain wall position in multiferroic heterostructures, Appl. Phys. Lett. **108**, 082401 (2016).

11 F. Zighem, D. Faurie, S. Mercone, M. Belmeguenai, and H. Haddadi, Voltage-induced strain control of the magnetic anisotropy in a Ni thin film on flexible substrate, J. Appl. Phys. **114**, 073902 (2013), arXiv: 1309.1417.

12 M. Weiler, A. Brandlmaier, S. Geprägs, M. Althammer, M. Opel, C. Bihler, H. Huebl, M. S. Brandt, R. Gross, and S. T. B. Goennenwein, Voltage controlled inversion of magnetic anisotropy in a ferromagnetic thin film at room temperature, New J. Phys. **11**, 013021 (2011), arXiv: 0810.0389.

13 S. Dwivedi, and S. Dubey, On dynamics of current-induced static wall profiles in ferromagnetic nanowires governed by the Rashba field, Int. J. Appl. Comput. Math **3**, 27 (2017).

14 N. L. Schryer, and L. R. Walker, The motion of 180° domain walls in uniform dc magnetic fields, J. Appl. Phys. **45**, 5406 (1974).

15 Y. Chen, H. Wang, X. Lou, H. Guo, X. Li, Q. Wang, H. Fan, and X. Tian, Vortex domain structures induced by strain gradient reduce ferroelectric brittleness, Acta Mech. Sin. **39**, 422428 (2023).

16 Y. Shi, B. Lei, and Z. You, Modeling of the near-field radiation of acoustically actuated magnetoelectric antennas, Acta Mech. Sin. **39**, 523120 (2023).

17 G. Consolo, and G. Valenti, Analytical solution of the strain-controlled magnetic domain wall motion in bilayer piezoelectric/magnetostrictive nanostructures, J. Appl. Phys. **121**, 043903 (2017).

18 G. Consolo, Modeling magnetic domain-wall evolution in trilayers with structural inversion asymmetry, Ricerche Matematica **67**, 1001 (2018).

19 G. Consolo, and G. Valenti, Magnetic domain wall motion in nanoscale multiferroic devices under the combined action of magnetostriction, Rashba effect and dry-friction dissipation, Atti della Accademia Peloritana dei Pericolanti-Classe di Scienze Fisiche, Matematiche e Naturali **96(S1)**, 3 (2018).

20 G. Consolo, S. Federico, and G. Valenti, Strain-mediated propagation of magnetic domain-walls in cubic magnetostrictive materials, Ricerche Matematica **70**, 81 (2021).

21 A. Hubert, and R. Schafer, Magnetic Domains: The Analysis of Magnetic Microstructures (Springer, Berlin, Heidelberg, 2008).

22 B. D. Cullity, and C. D. Graham, Introduction to Magnetic Materials (John Wiley & Sons, Hoboken, 2011).

23 W. Zhou, and Y. Zhou, Analysis of mechanical behavior on anisotropic cylindrical superconducting materials with inclusions, Acta Mech. Sin. **39**, 122168 (2023).

24 A. E. Clark, K. B. Hathaway, M. Wun-Fogle, J. B. Restorff, T. A. Lograsso, V. M. Keppens, G. Petculescu, and R. A. Taylor, Extraordinary magnetoelasticity and lattice softening in bcc Fe-Ga alloys, J. Appl. Phys. **93**, 8621 (2003).

25 M. Wuttig, L. Dai, and J. Cullen, Elasticity and magnetoelasticity of Fe-Ga solid solutions, Appl. Phys. Lett. **80**, 1135 (2002).

26 S. Maity, S. Dolui, S. Dwivedi, and G. Consolo, Domain wall dynamics in cubic magnetostrictive materials subject to Rashba effect and nonlinear dissipation, Z. Angew. Math. Phys. **74**, 23 (2023).

27 S. Maity, A. Halder, and S. Dwivedi, Role of nonlinear viscous dissipa-

tion on the magnetic domain wall motion in multiferroic heterostructures, Mech. Adv. Mater. Struct. 1 (2023).

28 Y. Hu, T. Cao, and M. Xie, Magnetic-structure coupling dynamic model of a ferromagnetic plate parallel moving in air-gap magnetic field, Acta Mech. Sin. **38**, 522084 (2022).

29 B. Wang, C. Chen, and Y. Shen, A micromechanics-based finite element model for the constitutive behavior of polycrystalline ferromagnets, Acta Mech. Sin. **22**, 257 (2006).

30 E. de Ranieri, P. E. Roy, D. Fang, E. K. Vehsthedt, A. C. Irvine, D. Heiss, A. Casiraghi, R. P. Campion, B. L. Gallagher, T. Jungwirth, and J. Wunderlich, Piezoelectric control of the mobility of a domain wall driven by adiabatic and non-adiabatic torques, Nat. Mater. **12**, 808 (2013).

31 A. Mougin, M. Cormier, J. P. Adam, P. J. Metaxas, and J. Ferré, Domain wall mobility, stability and Walker breakdown in magnetic nanowires, Europhys. Lett. **78**, 57007 (2007), arXiv: cond-mat/0702492.

32 B. Zhou, P. Khanal, O. J. Benally, D. Lyu, D. B. Gopman, A. Enriquez, A. Habiboglu, K. Warrilow, J. P. Wang, and W. G. Wang, Perpendicular magnetic anisotropy, tunneling magnetoresistance and spin-transfer torque effect in magnetic tunnel junctions with Nb layers, Sci. Rep. **13**, 3454 (2023), arXiv: 2210.14969.

33 A. Manchon, H. C. Koo, J. Nitta, S. M. Frolov, and R. A. Duine, New perspectives for Rashba spin-orbit coupling, Nat. Mater. **14**, 871 (2015), arXiv: 1507.02408.

34 O. V. Pylypovskyi, D. D. Sheka, V. P. Kravchuk, K. V. Yershov, D. Makarov, and Y. Gaididei, Rashba torque driven domain wall motion in magnetic helices, Sci. Rep. **6**, 23316 (2016), arXiv: 1510.04725.

35 Y. Xu, Y. Yang, K. Yao, B. Xu, and Y. Wu, Self-current induced spin-orbit torque in FeMn/Pt multilayers, Sci. Rep. **6**, 26180 (2016), arXiv: 1605.05135.

36 X. Zhang, Z. Xu, J. Ren, Y. Qiao, W. Fan, and Z. Zhu, Spin-transfer-torque induced spatially nonuniform switching in ferrimagnets, Appl. Phys. Lett. **124**, 012405 (2024).

37 C. K. Shahu, S. Dwivedi, and S. Dubey, Curved domain walls in the ferromagnetic nanostructures with Rashba and nonlinear dissipative effects, Appl. Math. Comput. **420**, 126894 (2022).

38 E. Martinez, The influence of the Rashba field on the current-induced domain wall dynamics: A full micromagnetic analysis, including surface roughness and thermal effects, J. Appl. Phys. **111**, 07D302 (2012).

39 P. B. He, Z. D. Zhou, R. X. Wang, Z. D. Li, M. Q. Cai, and A. L. Pan, Stability analysis of current-driven domain wall in the presence of spin Hall effect, J. Appl. Phys. **114**, 093912 (2013).

40 E. Martinez, S. Emori, and G. S. D. Beach, Current-driven domain wall motion along high perpendicular anisotropy multilayers: The role of the Rashba field, the spin Hall effect, and the Dzyaloshinskii-Moriya interaction, Appl. Phys. Lett. **103**, 072406 (2013).

41 S. M. Seo, K. W. Kim, J. Ryu, H. W. Lee, and K. J. Lee, Current-induced motion of a transverse magnetic domain wall in the presence of spin Hall effect, Appl. Phys. Lett. **101**, 022405 (2012), arXiv: 1202.3450.

42 J. Ryu, K. J. Lee, and H. W. Lee, Current-driven domain wall motion with spin Hall effect: Reduction of threshold current density, Appl. Phys. Lett. **102**, 172404 (2013), arXiv: 1303.6458.

43 A. El Hamdi, J. Y. Chauleau, M. Boselli, C. Thibault, C. Gorini, A. Smogunov, C. Barreteau, S. Gariglio, J. M. Triscone, and M. Viret, Observation of the orbital inverse Rashba-Edelstein effect, Nat. Phys. **19**, 1855 (2023).

44 C. Shen, R. Cai, A. Matos-Abiague, W. Han, J. E. Han, and I. Žutić, Rashba spin-orbit coupling enhanced magnetoresistance in junctions with one ferromagnet, Phys. Rev. B **107**, 125306 (2023), arXiv: 2303.00185.

45 C. K. Shahu, and S. Dubey, Transverse domain wall dynamics in hybrid piezoelectric/ferromagnetic devices, Math Methods App. Sci. **46**, 17020 (2023).

46 S. Dwivedi, Y. Priyobarta Singh, and G. Consolo, On the statics

47 C. K. Shahu, S. Dubey, and S. Dwivedi, Domain wall motion in multiferroic nanostructures under the influence of spin-orbit torque and nonlinear dissipative effect, Mech. Adv. Mater. Struct. **30**, 5047 (2023).

48 J. M. Hu, T. Yang, K. Momeni, X. Cheng, L. Chen, S. Lei, S. Zhang, S. Trolier-McKinstry, V. Gopalan, G. P. Carman, C. W. Nan, and L. Q. Chen, Fast magnetic domain-wall motion in a ring-shaped nanowire driven by a voltage, Nano Lett. **16**, 2341 (2016).

49 A. W. Rushforth, R. Rowan-Robinson, and J. Zemen, Deterministic magnetic domain wall motion induced by pulsed anisotropy energy, J. Phys. D-Appl. Phys. **53**, 164001 (2020).

50 C. K. Shahu, S. Dwivedi, and S. Dubey, Dynamics of curved domain walls in hard ferromagnets with nonlinear dissipative and inertial effects, Phys. D-NOnlinear Phenom. **448**, 133737 (2023).

51 G. Consolo, C. Currò, and G. Valenti, Curved domain walls dynamics driven by magnetic field and electric current in hard ferromagnets, Appl. Math. Model. **38**, 1001 (2014).

52 J. Y. Li, C. H. Lei, L. J. Li, Y. C. Shu, and Y. Y. Liu, Unconventional phase field simulations of transforming materials with evolving microstructures, Acta Mech. Sin. **28**, 915 (2012).

53 L. Thomas, M. Hayashi, X. Jiang, R. Moriya, C. Rettner, and S. S. P. Parkin, Oscillatory dependence of current-driven magnetic domain wall motion on current pulse length, Nature **443**, 197 (2006).

54 A. Goussev, R. G. Lund, J. M. Robbins, V. Slastikov, and C. Sonnenberg, Domain wall motion in magnetic nanowires: An asymptotic approach, Proc. R. Soc. A. **469**, 20130308 (2013), arXiv: 1310.4442.

55 S. Agarwal, G. Carbou, S. Labbé, and C. Prieur, Control of a network of magnetic ellipsoidal samples, Math. Control Relat. Fields **1**, 129 (2011).

56 J. A. Osborn, Demagnetizing factors of the general ellipsoid, Phys. Rev. **67**, 351 (1945).

57 G. Carbou, Stability of static walls for a three-dimensional model of ferromagnetic material, J. de Mathématiques Pures Appliquées **93**, 183 (2010).

58 S. Dwivedi, and S. Dubey, On the stability of static domain wall profiles in ferromagnetic thin film, Res. Math Sci. **6**, 1 (2019).

59 S. Zhou, Y. Wang, and Y. Liu, Modelling of magnetic stray fields in multilayer magnetic films with in-plane or perpendicular anisotropy, Magnetochemistry **8**, 159 (2022).

60 S. Jenkins, A. Meo, L. E. Elliott, S. K. Piotrowski, M. Bapna, R. W. Chantrell, S. A. Majetich, and R. F. L. Evans, Magnetic stray fields in nanoscale magnetic tunnel junctions, J. Phys. D-Appl. Phys. **53**, 044001 (2019), arXiv: 1907.11798.

61 Y. C. Shu, M. P. Lin, and K. C. Wu, Micromagnetic modeling of magnetostrictive materials under intrinsic stress, Mech. Mater. **36**, 975 (2004).

62 C. Y. Liang, S. M. Keller, A. E. Sepulveda, A. Bur, W. Y. Sun, K. Wetzlar, and G. P. Carman, Modeling of magnetoelastic nanostructures with a fully coupled mechanical-micromagnetic model, Nanotechnology **25**, 435701 (2014).

63 S. Federico, G. Consolo, and G. Valenti, Tensor representation of magnetostriction for all crystal classes, Math. Mech. Solids **24**, 2814 (2019).

64 S. Federico, A. Grillo, and S. Imatani, The linear elasticity tensor of incompressible materials, Math. Mech. Solids **20**, 643 (2015).

65 L. J. Walpole, Fourth-rank tensors of the thirty-two crystal classes: Multiplication tables, Proc. R. Soc. Lond. A **391**, 149 (1984).

66 W. P. Mason, Derivation of magnetostriction and anisotropic energies for hexagonal, tetragonal, and orthorhombic crystals, Phys. Rev. **96**, 302 (1954).

67 R. M. Bozorth, Magnetostriction and crystal anisotropy of single crystals of hexagonal cobalt, Phys. Rev. **96**, 311 (1954).

68 A. Hubert, W. Unger, and J. Kranz, Messung der magnetostriktionskonstanten des kobalts als funktion der temperatur, Z. Phys. **224**, 148 (1969).

69 V. Z. C. Paes, and D. H. Mosca, Field-induced lattice deformation

contribution to the magnetic anisotropy, J. Appl. Phys. **112**, 103920 (2012).

70 C. Eyrich, W. Huttema, M. Arora, E. Montoya, F. Rashidi, C. Burrowes, B. Kardasz, E. Girt, B. Heinrich, O. N. Mryasov, M. From, and O. Karis, Exchange stiffness in thin film Co alloys, J. Appl. Phys. **111**, 07C919 (2012).

71 M. Oogane, T. Wakitani, S. Yakata, R. Yilgin, Y. Ando, A. Sakuma, and T. Miyazaki, Magnetic damping in ferromagnetic thin films, Jpn. J. Appl. Phys. **45**, 3889 (2006).

72 N. Nakamura, H. Ogi, M. Hirao, and T. Ono, Elastic constants and magnetic anisotropy of Co/Pt superlattice thin films, Appl. Phys. Lett. **86**, 111918 (2005).

考虑Rashba效应及非线性耗散效应的混合压电-磁致伸缩结构中的应变诱导快速磁畴壁运动

Sumit Maity, Sarabindu Dolui, Sharad Dwivedi

摘要 本文主要目的是分析磁致伸缩材料薄层中磁畴壁的运动, 这类材料可以完美附着在厚压电器的上表面. 我们的分析中考虑了一类横观各向同性的六角形亚类磁致伸缩材料, 这些材料展示了结构反转非对称性. 为此, 我们利用了一维扩展Landau-Lifshitz-Gilbert方程描述在磁场、自旋极化电流、磁弹性效应、磁晶各向异性、Rashba场和非线性干摩擦耗散等因素影响下的磁化动力学. 通过标准的行波近似法, 我们推导出了最相关动态特性的解析表达式: 速度、迁移率、阈值、击穿和畴壁的传播方向, 包括稳态和进动动态状态. 我们的解析研究提供了如何有效控制磁畴壁运动的参数的见解. 解析结果的数值模拟与近期的观测结果定性上一致.